Influence of rift obliquity on fault-population systematics: results of experimental clay models

Amy E. Clifton [a,b,*], Roy W. Schlische [b], Martha O. Withjack [b], Rolf V. Ackermann [c]

[a] *Nordic Volcanological Institute, Grensasvegur 50, 104 Reykjavik, Iceland*
[b] *Department of Geological Sciences, Rutgers University, 610 Taylor Road, Piscataway, NJ 08854-8066, USA*
[c] *ExxonMobil Upstream Research Company, 3120 Buffalo Speedway, Houston, TX 77252-2189, USA*

Abstract

We use clay models to simulate how fault population systematics vary as a function of rift obliquity. Rift obliquity is related to the acute angle, α, between the rift trend and the displacement direction, so that the value of α is inverse to the degree of obliquity. The range of azimuths in a fault population increases as rift obliquity increases (i.e. as α decreases). The length of the longest faults, the sum of fault lengths, and the width of the deformed zone all increase as rift obliquity decreases (i.e. as α increases). The majority of faults in our models are segmented and have highly tortuous traces. Tortuosity is maximum when $\alpha = 30°$ as segments of widely varying azimuth link during fault growth. Significant changes occur in the fault patterns between $\alpha = 30°$ and $\alpha = 45°$. At $\alpha = 30°$ two fault populations of equal importance develop in the center of the rift zone, one approximately rift-parallel and the other displacement-normal. Between $\alpha = 30°$ and $45°$, the number of faults more than doubles, and between $\alpha = 45°$ and $60°$, summed fault length more than doubles. Fault patterns for all models are fractal, with fractal dimensions that increase with increasing α and that are comparable to those found in the field. Fault populations are not multi-fractal because the cumulative frequency distributions of fault lengths do not generally follow a power-law relationship. An exponential distribution best describes the data for whole faults, with the characteristic length increasing with increasing α. Segment lengths also follow an exponential distribution with characteristic length varying very little with α. The fault patterns in our models resemble the spatial pattern of brittle deformation observed at oblique mid-ocean ridge segments and are similar in geometry to those in oblique continental rift basins. At the rift margins, tensional stresses are modulated and reoriented by a secondary stress field related to a change in boundary conditions, resulting in the formation of two distinct sub-populations of faults during oblique rifting. © 2000 Elsevier Science Ltd. All rights reserved.

1. Introduction

During the past 10 years, numerous studies have led to a new and better understanding of how faults grow and how fault populations evolve in extensional tectonic settings (Cowie and Scholz, 1992; Cowie et al., 1993a; Dawers, 1996; Ackermann and Schlische, 1997; Ackermann et al., 1997; Cowie, 1998). Most previous studies have focused on simple orthogonal extension in order to determine the basic mechanical processes at work during fault population evolution. This study applies many of the same techniques to oblique extension. With oblique extension, the trend of the deformed zone (referred to hereafter as rift trend) is oblique to the displacement direction. The acute angle, α, between the rift trend and the displacement is inversely related to the degree of obliquity, so that a highly oblique rift has a low value of α (Fig. 1) (Withjack and Jamison, 1986).

Quantifying brittle deformation during oblique extension is important to understand how fracture populations evolve in a range of tectonic settings. Rift basins commonly localize along a pre-existing tectonic fabric that is oriented obliquely to the absolute displa-

* Corresponding author. Fax: +354-562-9767.
E-mail address: amy@norvol.hi.is (A.E. Clifton).

cement direction (e.g. Lindholm, 1978; Angelier and Bergerat, 1983; Morley, 1995). Changes in the direction of plate motion may also impose oblique spreading on mid-ocean ridge segments (e.g. Dauteuil and Brun, 1993). Field studies in both continental and ocean-ridge environments describe a complex interaction between displacement-normal and rift-parallel structures in oblique rift zones such as the Gulf of California (Withjack and Jamison, 1986; Umhoefer and Stone, 1996), the Gulf of Aden (Withjack and Jamison, 1986), the Hartford basin of eastern North America (Clifton, 1987; deBoer and Clifton, 1988), the Malawi rift of east Africa (Chorowicz and Sorlien, 1992), the Reykjanes Ridge south of Iceland (Murton and Parson, 1993; McAllister et al., 1995), the Mohns Ridge north of Jan Mayen (Dauteuil and Brun, 1996), and several grabens in the northern North Sea (Færseth et al., 1997). In rifts oriented sub-perpendicular to the displacement direction, some fault populations have a fractal scaling that can be described by a power-law size distribution (Cowie et al., 1993b). Studies by Hatton et al. (1994) and Ackermann et al.

(1997) indicate a lower and upper limit to fractal scaling, respectively. Preliminary work on experimental models of oblique extension suggest that the size distribution of faults varies with α (Clifton and Schlische, 1997; Clifton et al., 1998).

Although they are not perfectly scaled reproductions of geological conditions (e.g. they are relatively homogeneous and isotropic whereas rock is relatively heterogeneous and anisotropic), results from analyses of experimental models can be used to guide and support real world investigations. Experimental models are ideal for studying oblique extension because the boundary conditions can be precisely known and controlled. Experimental models allow us to observe and record the temporal evolution of deformation, whereas in nature only the final deformation state is observable. Experimental models also allow us to examine the entire (visible) population of faults resulting from specific boundary conditions. Previous experimental modeling studies of oblique extension have focused on the geometry and spatial distribution of the resulting fault patterns in clay, sand, and sand over putty (Withjack and Jamison, 1986; McClay and White, 1995; Tron and Brun, 1991, respectively). Fault geometries produced in these experiments were quite similar despite differences in the modeling media and experimental set-up. This study quantifies changes in fault-population systematics as the rift angle decreases from $\alpha = 90°$ (pure extension) to $\alpha = 0°$ (pure strike slip). We obtained a large (> 200) number of faults in each model, enabling us to characterize accurately the fault populations by integrating data on strain accommodation, fault geometries, scaling relationships, and the size and spatial distribution of faults.

2. Experimental procedures

The modeling apparatus (Fig. 1) has a stationary base plate and four vertical walls, three fixed and one moveable. The dimensions of the apparatus are approximately 61 cm × 60 cm prior to deformation. Following Withjack and Jamison (1986) a metal plate is attached to the moving wall. The geometry of the metal plate varies in the models to simulate a range of oblique extension. In this series of models, the angle, α, between the rift axis (oriented parallel to the edge of the metal base plate) and the direction of displacement is varied in 15° increments between 0° (left-lateral strike-slip) and 90° (pure extension). A latex sheet 6-cm wide is centered over the edge of the metal plate and the base plate and is securely attached. A 2.5-cm-thick layer of wet clay overlies the metal plate, latex sheet and base plate. The clay (40% water by weight) is composed of powdered kaolin ≤ 0.1 mm in diameter. Its density is approximately 1.65 g/cm^3, it has a
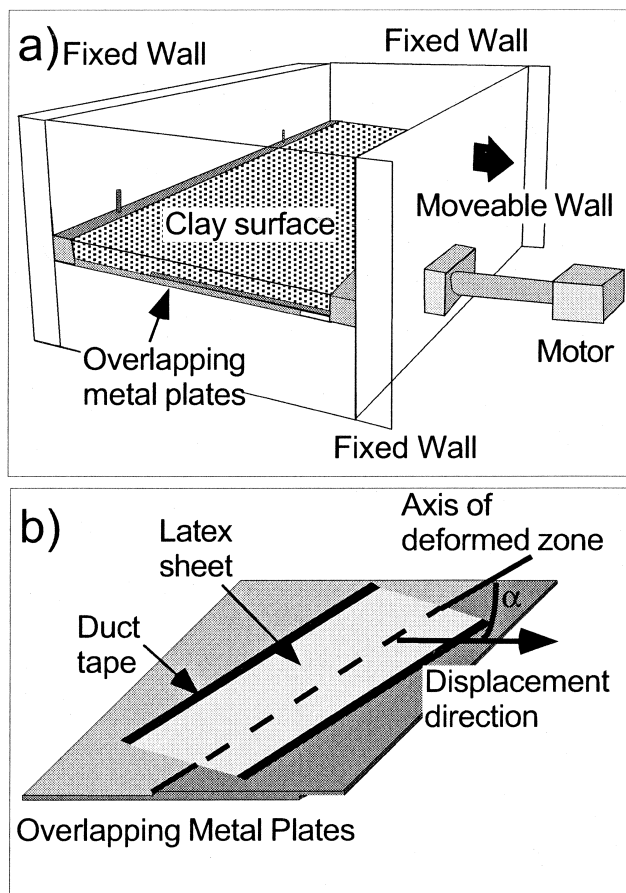

Fig. 1. (a) Experimental apparatus. (b) Detail of apparatus surface without clay layer, showing that α is defined as the acute angle between the rift axis and the displacement direction (Withjack and Jamison, 1986).

low cohesion (∼50 Pa), and it has a coefficient of internal friction of about 0.5.

The cohesion and coefficient of internal friction of the wet clay are appropriate to ensure dynamic similarity between the models and natural analogs (e.g. Hubbert, 1937). The cohesion of rock is about 10^4–10^5 times greater than that of the modeling materials. The dimensions of the model are scaled down by a factor of 10^{-4}–10^{-5} from those in the real world, such that 1 cm in the models is equivalent to 100–1000 m in nature. The wet clay represents strong rock that deforms by both distributed cataclasis and localized cataclastic faulting (i.e. upper crustal conditions; Withjack and Callaway, 2000).

For each model run, the moving wall is displaced a total of 6 cm at a constant rate of 3 cm/h. As the wall moves, the attached metal plate also moves and the latex stretches uniformly, imposing distributed deformation to the overlying layer of wet clay, and producing a rift zone slightly wider than the latex sheet. We photographed the model surface, using at least two different lighting directions, every 0.25 cm of displacement. In this paper, we present results of the analysis at a single displacement increment (3.5 cm) to determine how fault attributes vary with rift angle.

3. Data collection

We selected a rectangular study area of 650 cm^2 centered on the rift zone for each model. The size and position of the study area were chosen to eliminate edge effects caused by the outer walls of the apparatus and the short ends of the latex sheet. Defining the edge effect was based solely on visual inspection. The edge effect was considered absent or minimal when the fault pattern became consistent. Use of photographic images of the model surfaces with two different lighting directions permitted accurate tracing of both the hanging wall and footwall cutoffs of brightly lit fault scarps (see Fig. 2). We drew fault trace maps for each model at the 3.5-cm displacement increment (Fig. 3). At this displacement, fault populations on all models are sufficiently large to perform statistical analyses. Data collected from the fault trace maps for each α angle consist of the fault trend (measured from tip to tip), tip-to-tip length, and fault trace perimeter.

In analyzing the images of the model surfaces, as is also true in interpreting field and seismic data, determining the true length of faults can be problematic. In our experiments the uncertainty is primarily a result of photographic resolution which leads to three problems: 1) Faults smaller than 0.2–0.3 cm in length do not show up clearly on the images so that data for cumulative frequency of fault lengths are truncated at the small end. 2) On the black-and-white images, fault scarps facing the lighting direction appear white, whereas the area around the majority of fault tips appears gray. In many cases, we interpret the aureole of light gray at the fault tip as either a damage zone or a fold propagating in advance of the fault (Fig. 4d). The transition from white fault tip to gray aureole is commonly subtle on the images, indicating that a portion of the dataset for fault lengths is censored. However, in the majority of cases, using images from both lighting directions enabled us to confidently identify fault tips. 3) Image quality varies somewhat from one model run to the next and even within the study area of a given model. Where hanging wall blocks have experienced considerable rotation or where grabens have formed on the model, some areas are in shadow from both lighting directions and small faults cannot be seen.

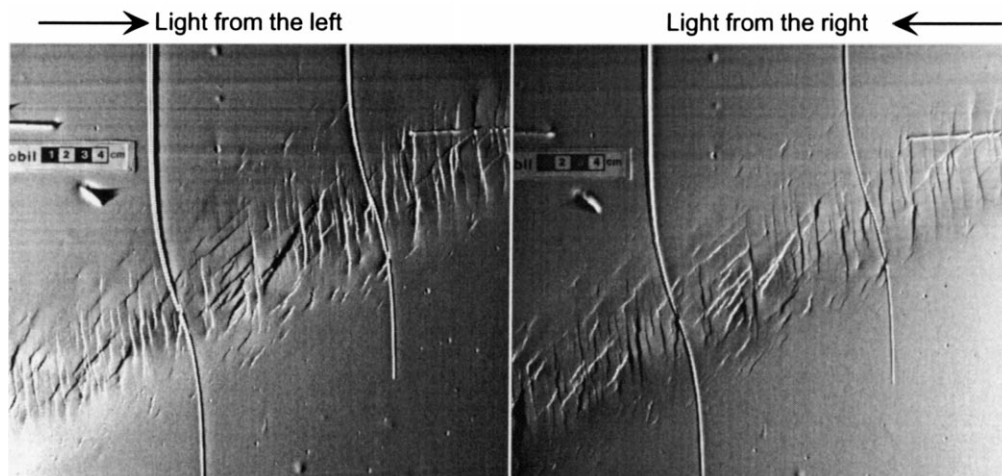Uncertainty is greatest when determining the lengths

Fig. 2. Photographs of the surface of model $\alpha = 30°$ shown for two different lighting directions. Brightly lit fault scarps face the lighting direction. The moving wall is to the right. Thick lines on model surface are trowel marks.

of faults on the $\alpha \leq 15°$ models. The predominantly strike-slip faults in these models have significantly less vertical displacement than the normal faults, making them more difficult to distinguish on the images. Therefore, it is quite possible that faults on these models were undersampled at all scales. As is also the case with field data, there is no way to be certain that we are sampling the maximum dimension of any given fault, and it is likely that some faults that are smaller than the thickness of the model have not yet broken through to the surface.

Observation of the models as they evolved confirmed that most faults grow primarily by linkage. As a result, the majority of faults in this study are segmented (e.g. Trudgill and Cartwright, 1994). During the generation of fault trace maps, segment boundaries were identified using the following criteria: 1) abrupt changes in fault strike (Fig. 4d); 2) abrupt changes in fault displacement profiles resulting in displacement deficit in the middle of a fault (Fig. 4c); 3) abandoned splays (Fig. 4b); and 4) stranded footwall or hanging-wall rider blocks (Fig. 4a). Any of these criteria alone, except for the first criterion, can indicate a segment boundary. Inspection of images from consecutive displacement increments shows that, when faults grow by tip propagation, the fault tip may bend into the damage zone and abrupt changes in strike commonly result. Therefore, the first criterion must be used in conjunction with other criteria. Field and laboratory studies (e.g. Schlische and Anders, 1996; Withjack,
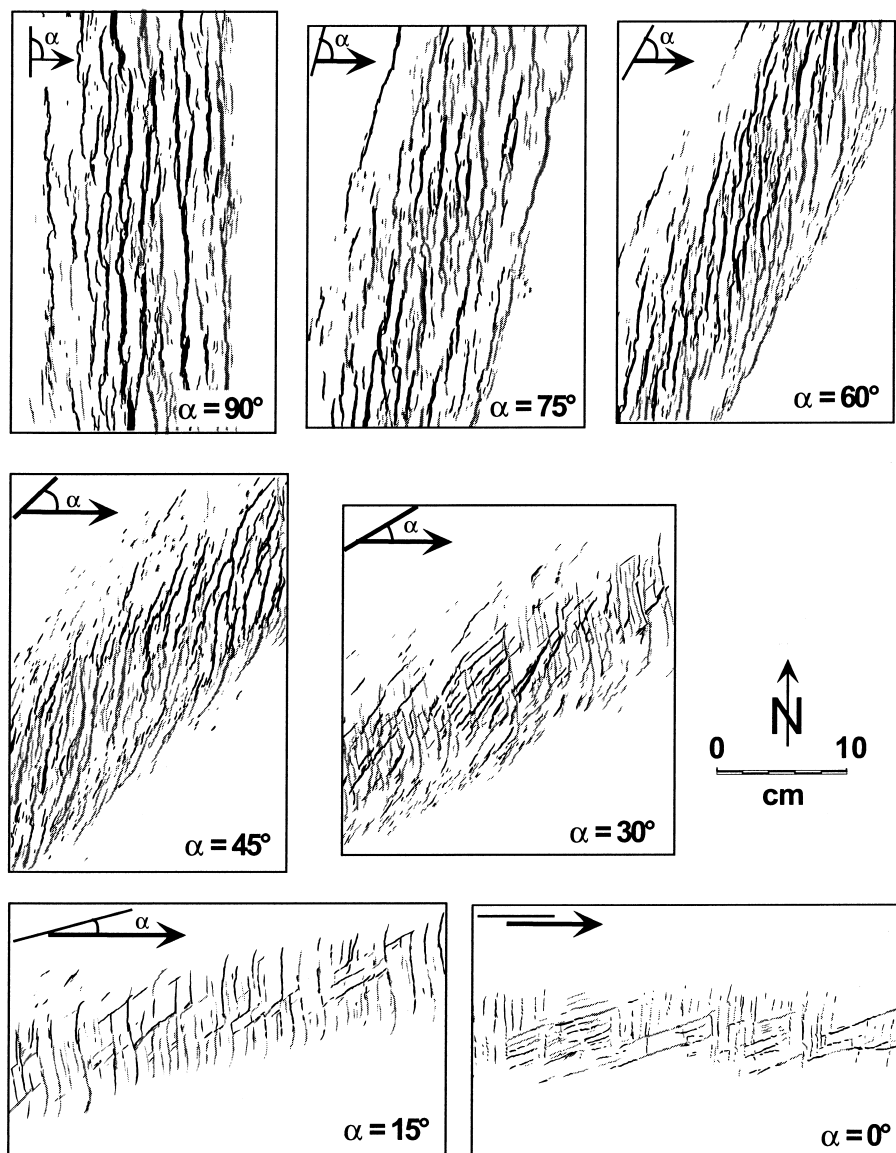

Fig. 3. Fault trace maps. Black fault surfaces face the moving wall and dip to the right. Gray faults face away from the moving wall and dip to the left.

unpublished data) indicate that the displacement deficit incurred during fault linkage is commonly preserved during subsequent fault growth. Consequently, we were able to identify fault segment boundaries with a high degree of confidence.

Sense of slip along faults in the models was determined qualitatively by visual inspection during growth of the models and by offset of passive markers (e.g. linear scrape marks and air bubbles) on the model surface. A system of strain markers (e.g. a grid) was not placed on the model surfaces because previous work had indicated that they commonly act as anisotropies that influence the direction of fault propagation. During growth of the models, it was occasionally possible to see slickenlines on fault surfaces. Unfortunately, these do not show up on the photographic images.
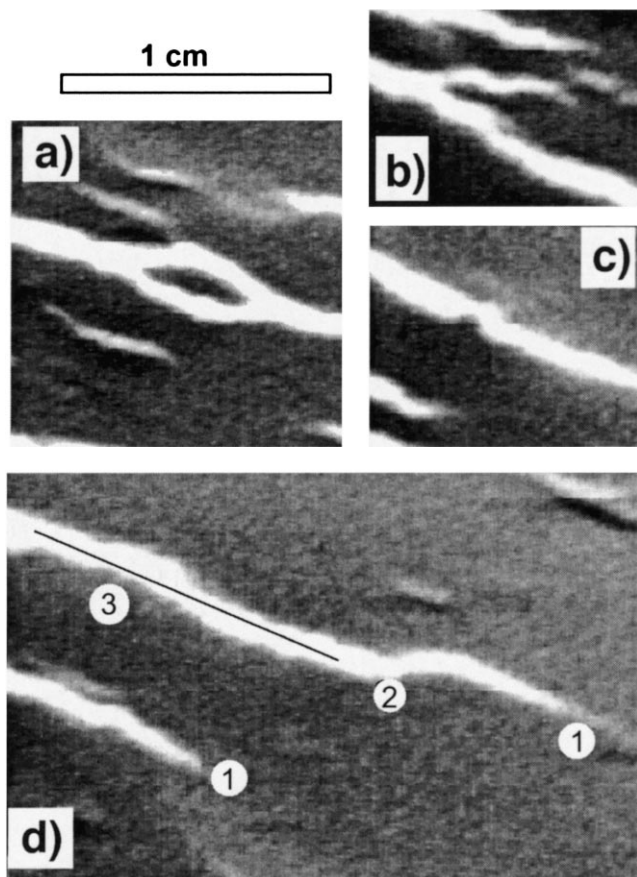

Fig. 4. Criteria for identifying segment boundaries: (a) abandoned rider block; (b) abandoned splay; (c) displacement deficit in the center of the fault trace; (d) trace of a long fault for which 1 denotes gray aureoles at two fault tips, 2 denotes a change in strike that may be due to tip propagation rather than linkage and 3 denotes a part of the fault trace with a flat displacement profile.

4. Data

4.1. Description of fault trace maps

The pattern of faulting changes considerably as the rift zone becomes increasingly oblique, with the most noticeable change occurring between $\alpha = 45°$ and $30°$ (Fig. 3). However, there are many similarities in all of the fault-trace maps. Most faults exhibit the characteristics associated with segmented fault systems (e.g. Trudgill and Cartwright, 1994; Cartwright et al., 1995), including flat displacement profiles (3 in Fig. 4d), many abandoned splays (Fig. 4b), stranded rider blocks (Fig. 4a), and tortuous fault traces. Relay ramps are evident where fault tips approach each other, and horst and graben structures are also common. In most models, faults form clearly recognizable dip domains in which faults with a uniform dip direction are clustered together. At the boundaries of dip domains, the fault patterns become complex, resembling the accommodation zones described in the Gulf of Suez (e.g. Moustafa, 1996) and Mid-Atlantic Ridge (Mutter and Karson, 1992).

On all maps for $\alpha \geq 45°$, faults along the borders of the rift form a distinct zone separated in space from faults within the rift. These border-zone faults have a trend that is slightly oblique to rift-parallel, whereas faults within the rift trend slightly oblique to the displacement-normal direction. This pattern of faulting is similar to that described at oblique mid-ocean ridge segments such as the Mohns Ridge (Dauteuil and Brun, 1996) and the Reykjanes Ridge (McAllister et al., 1995).

4.2. Fault geometry

The most obvious difference between oblique and orthogonal rift zones is the range of fault azimuths. We measured azimuth tip-to-tip for all continuous fault traces and obtained results that were consistent with the findings of Withjack and Jamison (1986). Our models confirm that, as α decreases from $90°$, the range of fault azimuths increases steadily, with the greatest change occurring once again between $\alpha = 45°$ and $30°$. Also, the predominant fault trend shifts gradually from displacement-normal to oblique with respect to both the displacement direction and the rift trend (see Fig. 5). When $\alpha = 45°$, the predominant fault trend lies exactly halfway between the rift trend and the displacement-normal trend. A major change occurs at $\alpha = 30°$, where two distinct peaks appear in the histogram of azimuths, indicating that there are two discrete subpopulations of faults, one approximately displacement-normal and the other striking rift-subparallel (i.e. $\leq 20°$ oblique to the rift trend). This also represents a change in the type of faulting, from

exclusively dip-slip to a combination of dip-slip, oblique-slip and strike-slip faulting. As α decreases from 30° towards 0°, the distance between the peaks increases, and the relative proportion of strike-slip faulting increases.

For α ≥ 45°, the longest faults have an azimuth that coincides with the peak of the histogram (Fig. 6) whereas the shortest faults span the entire range of azimuths within the model. For α = 30° and 15°, the longest faults have a displacement-normal trend whereas most rift-subparallel faults are short. For α = 0°, the longest faults are approximately rift-parallel whereas the short faults range in azimuth from 000° (i.e. displacement-normal) to 345°.

4.3. Spatial pattern of faults

Between α = 45° and α = 90°, faults with a rift-subparallel trend are found primarily at the rift margins. As α approaches 90°, these faults begin to link to form long, en-échelon border-fault arrays. At α = 90°, a single border fault has formed (Fig. 3). Between α = 45° and α = 75°, faults in the center of the rift zone have a trend that is oblique to displacement-normal. The obliquity of that trend decreases as α approaches 90°. For α ≤ 30°, rift-subparallel faults that strike ≤ 20° oblique to the rift trend are predominant both in the center of the rift and at the rift margins, and displacement-normal faults cross the rift zone. As α increases, the width of the deformed zone at the surface of the model increases (Fig. 7).

We measured fault spacing along scanlines oriented parallel to the displacement direction for models of α = 45° through 90° (Fig. 8). Brittle deformation in these models is dominated by faulting along displacement-normal faults. Results show that mean fault spacing increases with α. The most likely reason for this is that the longer faults in the less oblique models have larger stress-reduction shadows (e.g. Ackermann and Schlische, 1997) in which new faults cannot form. The
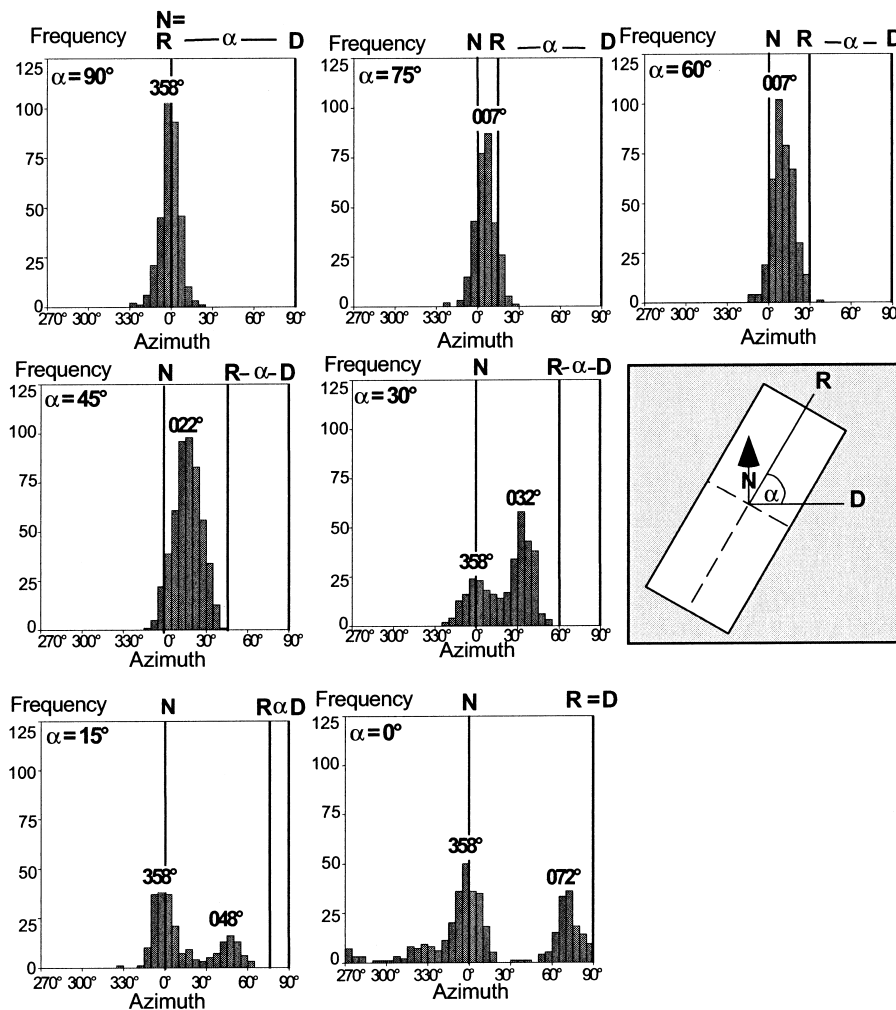

Fig. 5. Histograms of fault azimuth for all models. *R* is the trend of the rift axis for each α angle; *D* is the trend of the displacement direction, defined as 090°; *N* is the displacement-normal direction defined as 000°.

standard deviation of spacing also increases, indicating that spacing becomes somewhat less regular as α increases. For all models, the standard deviation is close to or greater than the mean. The high standard deviation is primarily a result of a zone of no faulting which lies between faults on the rift borders and those in the center of the rift.

The software package Benoit (TruSoft International, 1997) was used to investigate how the fractal dimension of the map pattern varies with α, and to determine whether the spatial patterns of faults in this study are multifractal. The fractal dimension is a quantification of the degree to which the map pattern is space-filling. A single straight line on a map would yield a fractal dimension of 1, whereas a completely filled map would yield a fractal dimension of 2 (Fig. 9). Benoit uses a box counting algorithm, which counts the number of boxes necessary to cover a dataset of points (pixels). Box size is varied geometrically within a range determined by the smallest and the largest dis-

tance between points on the fault maps. The program calculates two fractal dimensions, the capacity dimension D_c, which simply counts the number of occupied boxes, and the information dimension, D_i, which is D_c weighted by the normalized mass of points (pixels) present in each box. The log of the box size is then plotted against the log of the number of occupied boxes (or the weighted number of occupied boxes). If the data fall on a straight line, the map pattern is considered to be fractal and the slope of that line is the fractal dimension. Values for D_c and D_i in this study (Fig. 10) fall between 1.35 and 1.64, consistent with values found for fault patterns in the field (Aviles et al., 1987; Okobu and Aki, 1987; Hirata, 1989). Both D_c and D_i increase between $\alpha = 0°$ and $\alpha = 45°$, reflecting the fact that the fault maps become increasingly space filling. Above $\alpha = 45°$ values of D_c and D_i level off at 1.62 and 1.64, respectively, consistent with a theoretical D value of 1.65 derived by Takayasu (1986) for a percolating crack network and an upper limit of
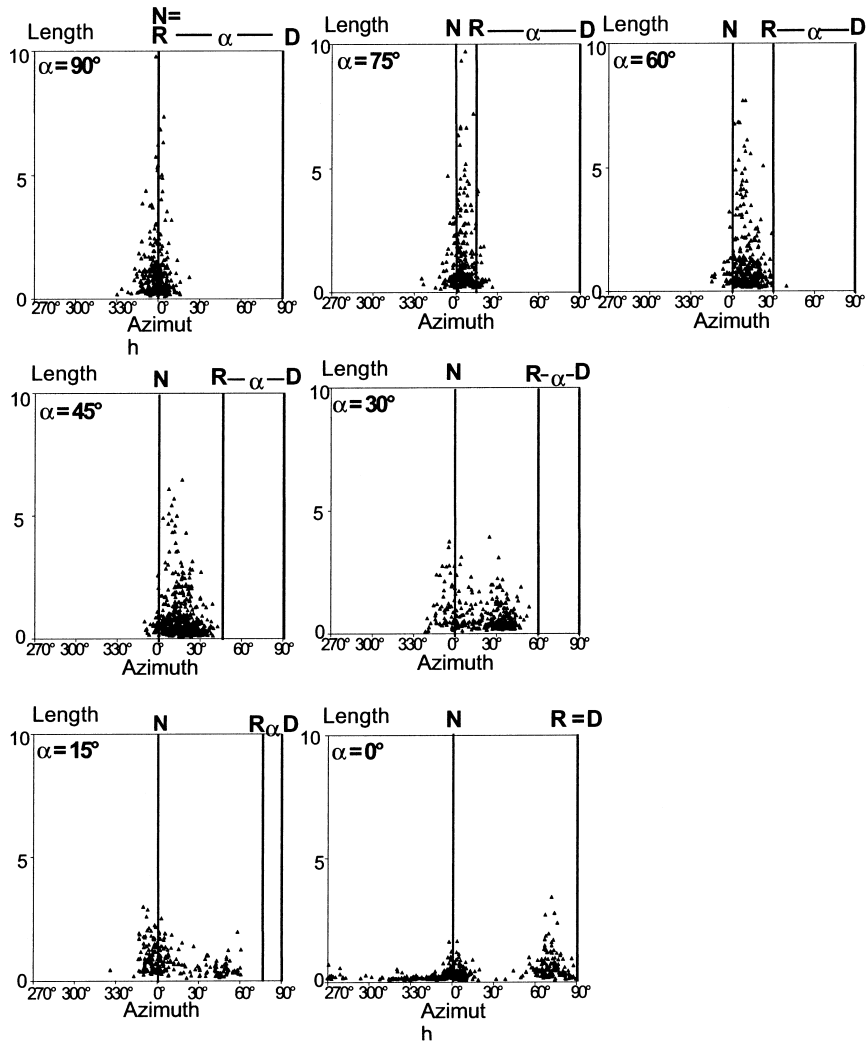

Fig. 6. Fault length vs. azimuth for all models. Letters the same as in Fig. 5.

$D = 1.6$ for branching fault networks in central Japan (Hirata, 1989).

Multifractality is an indicator of spatial clustering. Cowie et al. (1995) describe a multifractal set as one which has a power-law cumulative frequency of lengths superimposed on a fractal map pattern. The closer in value D_c and D_i are, the less multifractal the data are considered to be. Our oblique models cannot be considered multifractal because D_c and D_i are nearly equal for all values of α (see Fig. 10). This is consistent with our results for cumulative frequency distribution of fault lengths (see Section 4.6).

4.4. Fault-related strain

We measured fault-related strain for models of $\alpha \geq 45°$ along scan-lines oriented parallel to the displacement direction at the model surface. The width of each fault polygon is approximately equivalent to the heave on the fault. Thus, the sum of the widths of the fault polygons can be used to calculate fault-related strain. However, for models with strike-slip faults, ($\alpha \leq 30°$), the assumption that fault heave is related to strain is not valid.

The amount of extensional strain imposed at the base of our models varies according to:
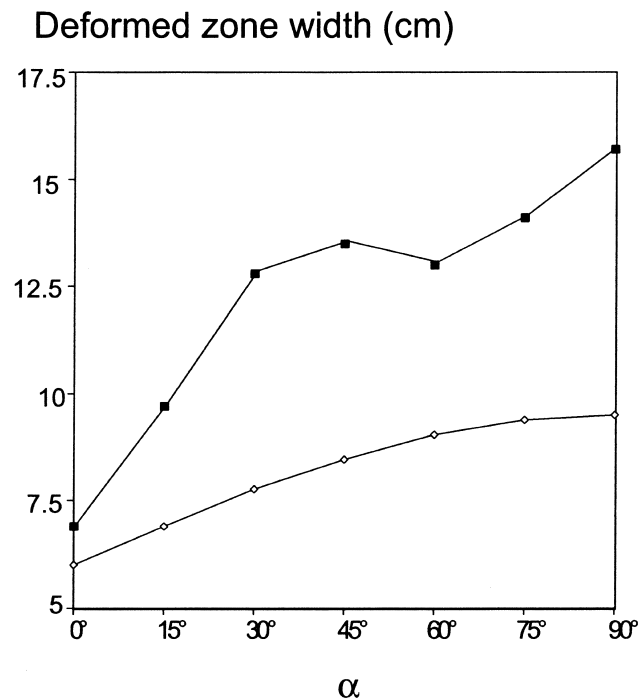
$$\varepsilon_{xx} = \frac{d}{u} \sin \alpha \qquad (1)$$

Deformed zone width (cm)

Fig. 7. Variation with α in width of the deformed zone at the clay surface (black squares) and at the base of the model (open diamonds).

centimeters
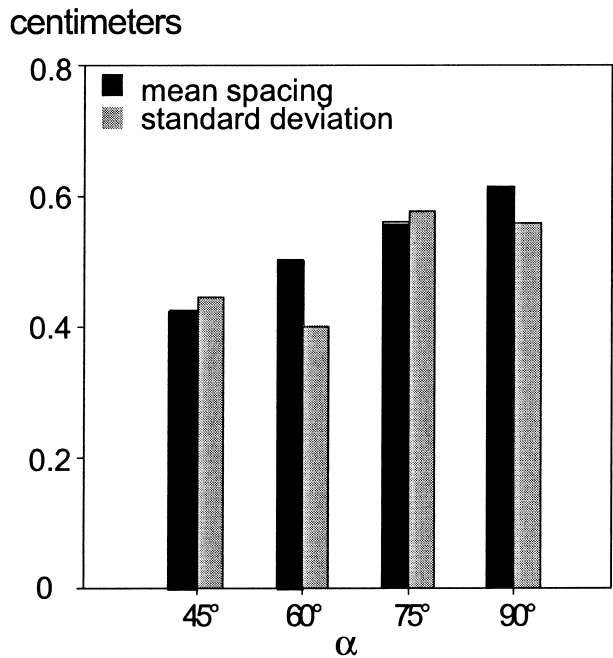

Fig. 8. Bar graph of mean fault spacing (black) and standard deviation of fault spacing (gray).

(Withjack and Jamison, 1986), where ε_{xx} represents extensional strain in the displacement direction, u is the original width of the rift and d is the distance that the rift edge has been displaced. Despite the increase in imposed strain with increasing α, the amount of strain attributable at the surface to brittle faulting remains almost constant and only represents between 30% and 50% of the imposed strain (Fig. 11). These results are consistent with conclusions of Kautz and Sclater (1988), who observed that as much as 50% or more of strain is accommodated by faults that fall
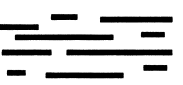

Fig. 9. Examples of map patterns with different fractal dimensions.
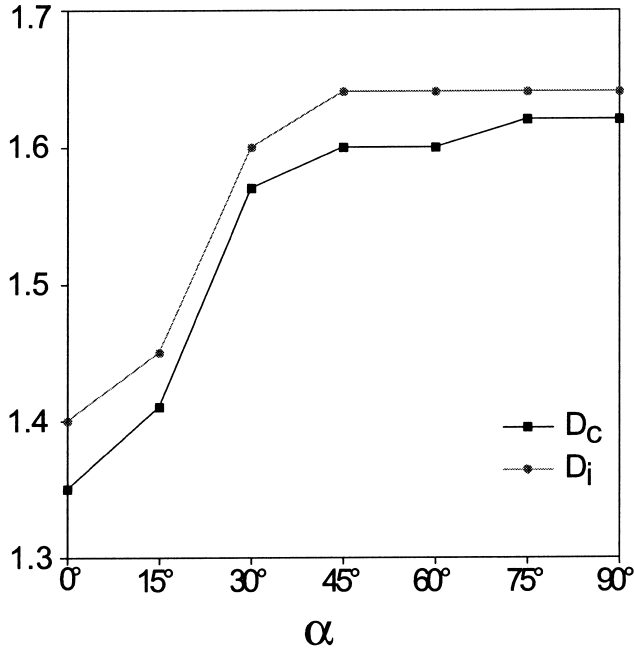
fractal dimension

Fig. 10. Graph of the capacity dimension (D_c) and the information dimension (D_i) as a function of α, as calculated by Benoit software.

below the resolution of detection methods. They suggest that the amount of 'hidden extension' is a function of both the minimum amount of observable
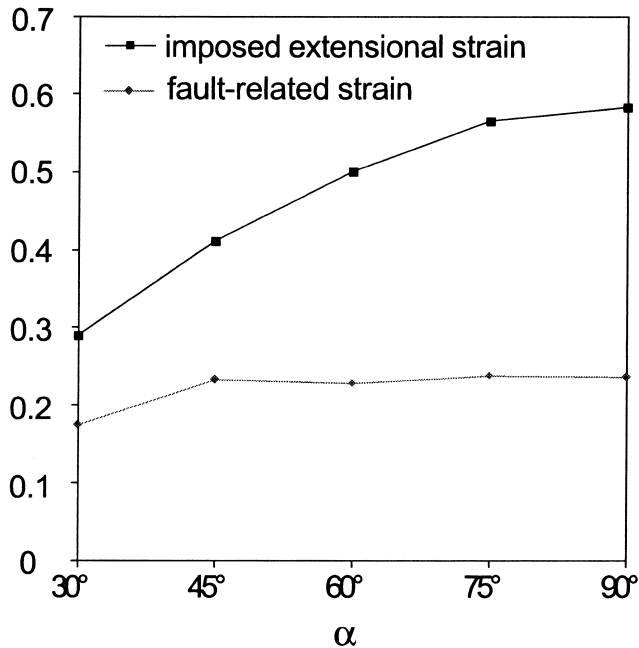
strain

Fig. 11. Graph showing how imposed extensional strain in the displacement direction (square symbols) compares with fault related strain (diamond symbols) for α > 30°.

slip and the grain size of the deformed material. In our clay models, this represents over two orders of magnitude of fault size on which slip is occurring below the detection limit. Our results suggest that the amount of hidden extension is greater in rifts with higher α values, but it is not clear whether this is due to differences in the amount of extensional strain, differences
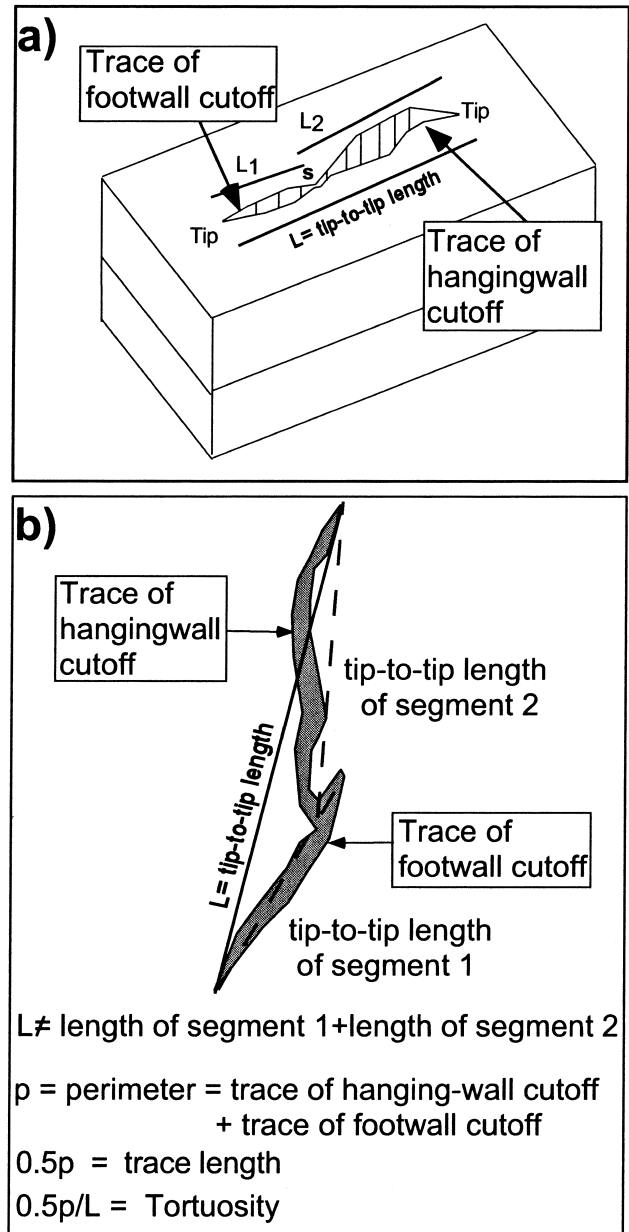
Fig. 12. (a) Diagram showing hanging wall and footwall cutoffs along a segmented fault. L_1 and L_2 are tip-to-tip lengths of individual segments, whereas L is the tip-to-tip length of the entire fault. s is the segment boundary. Note that tip-to-tip lengths and azimuths of segments do not equal that for the entire structure. Note too that the trace lengths defined by the hanging wall and footwall cutoffs are significantly longer than tip-to-tip lengths. Note displacement deficit at s. (b) Diagram defining fault tortuosity as the ratio of fault trace length to tip-to-tip length.

in fault geometry or both. Future work is required to seek the answer.

4.5. Fault length

Any continuous fault trace on the model surface is considered to be a single fault whose length can be measured as either trace length or tip-to-tip length (Fig. 12a). The measurement of trace length is more sensitive to resolution than the tip-to-tip length. Therefore, all length measurements in this study are made tip-to-tip. The ratio between fault trace length and tip-to-tip length is defined here as fault tortuosity (Fig. 12b). Tortuosity values fall between 1 for a perfectly straight line, and infinity for an infinitely tortuous fault trace. It is a function of both the degree of fault linkage and the variation of azimuth within the total population. With the exception of $\alpha = 0°$, tortuosity tends to increase with fault length within a given model. Average tortuosity is maximum when $\alpha = 30°$ (Fig. 13). In this model, extensional strain is accommodated by two sub-populations of oblique-slip normal faults which interact, particularly in the center of the rift, by linking to form long, zigzag faults. Despite the fact that the range of azimuths is even greater in the $\alpha = 15°$ and $0°$ models, the two sub-populations do not link to the same degree. Instead, strain is partitioned between two sets of predominantly strike-slip faults.

Several parameters related to fault length clearly vary with α, but each in a different manner (Fig. 14).
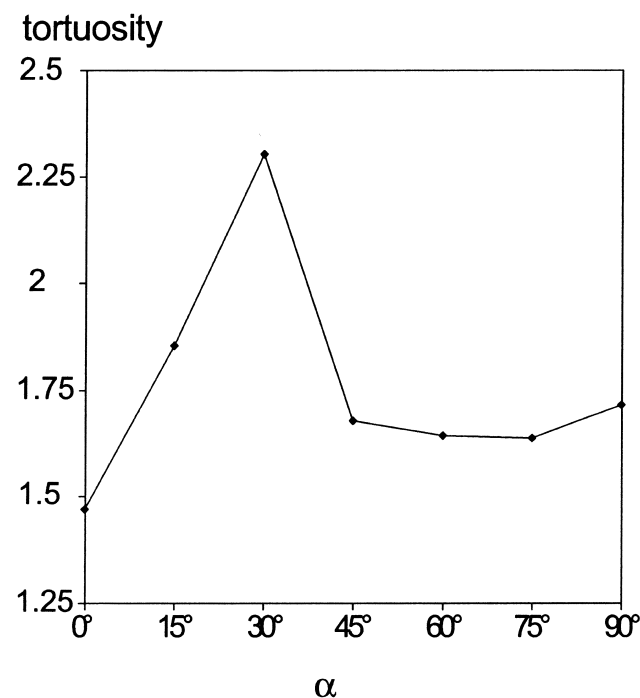
The length of the fault at the 95th percentile of all lengths (L_{95}) increases steadily from $\alpha = 0°$ to $90°$. Summed fault length rises steeply to a maximum value at $\alpha = 45°$ and then levels off. Data for the number of faults in each model rise and fall apparently unsystematically. When these parameters are normalized by the study area affected by faulting, changes in summed fault length and number of faults follow the same pattern, indicating that they are closely related. The $\alpha = 0°$ model has an anomalously high number of faults, due to the highly discontinuous nature of the strike-slip faults that occur in a very narrow deformed zone. Between $\alpha = 15°$ and $90°$, both the number of faults and summed fault length increase to a maximum at $\alpha = 45°$, then decrease for $\alpha = 60°$ and $75°$ before increasing again at $\alpha = 90°$. This pattern is most probably related to varying degrees of nucleation vs. linkage as α increases. Faults nucleate more slowly in the highly oblique models, while at the same time, linkage is limited by fault geometry. Conversely, faults nucleate readily in the less oblique models whereas most fault growth is accomplished by linkage. In these models, rift geometry is the primary factor limiting fault growth. When $\alpha = 90°$ (i.e. pure orthogonal rifting), fault growth is relatively unrestricted.

4.6. Cumulative frequency of lengths

Fault-scaling relationships have been used to estimate the relative numbers of faults that fall below the resolution of detection methods, to determine the aggregate properties of fault populations, to understand the process of fault population evolution in space and time, and to infer aspects of the underlying physical process of fault growth (Cowie et al., 1996). Previous workers have proposed that an exponential distribution of sizes with the form

$$N(L) = N_{T}e^{-\lambda L} \qquad (2)$$

characterizes fault populations both at the earliest stages of their evolution, when nucleation of new faults exceeds growth of existing faults (Cowie et al., 1995) and again after the largest faults have exceeded the thickness of the brittle layer (Ackermann et al., 1997). N is the total number of faults with dimensions greater than or equal to some length (L), N_T is the total number of measurements, and λ is a scaling parameter that is the inverse of the characteristic length (L_c). Between those extremes, a power-law distribution of sizes is expected such that

$$N(L) = aL^{-C} \qquad (3)$$

where a is related to the total number of measurements and C is the power-law exponent. A power-law distribution of sizes is indicative of self-similar fault growth

tortuosity

Fig. 13. Variation of average tortuosity with α? Values of tortuosity are normalized by fault length.

and scaling (Main, 1996). Sornette et al. (1990), Cowie et al. (1995) and Cladouhos and Marrett (1996) suggested that the power-law exponent of a given fault population should decrease as the population evolves and large faults accommodate increasingly more strain.

We eliminated measurements at the small end of the dataset (left-hand truncation of Pickering et al., 1995), recognizing that too many small faults fall below the resolution of the imaging technique, and plotted the data in log-linear space. For models of $\alpha \geq 30°$ we are confident that long faults were thoroughly sampled and that, therefore, these data should not be con-

sidered censored. There is greater uncertainty of this for models of $\alpha \leq 15°$ because of the lack of vertical offset along strike-slip faults. Cumulative frequency plots for all values of α show that all of our data are better fit by an exponential distribution than by a power-law, with the possible exception of $\alpha = 60°$ and $90°$ (Fig. 15). However, even for those models, a power-law distribution does not describe the whole dataset. In fact, there appears to be a bimodal distribution that may indicate two sub-populations that scale differently. Wojtal (1996) and Ackermann and Schlische (1997) also observed two fault subpopulations in outcrop studies that appear to be scaling dif-
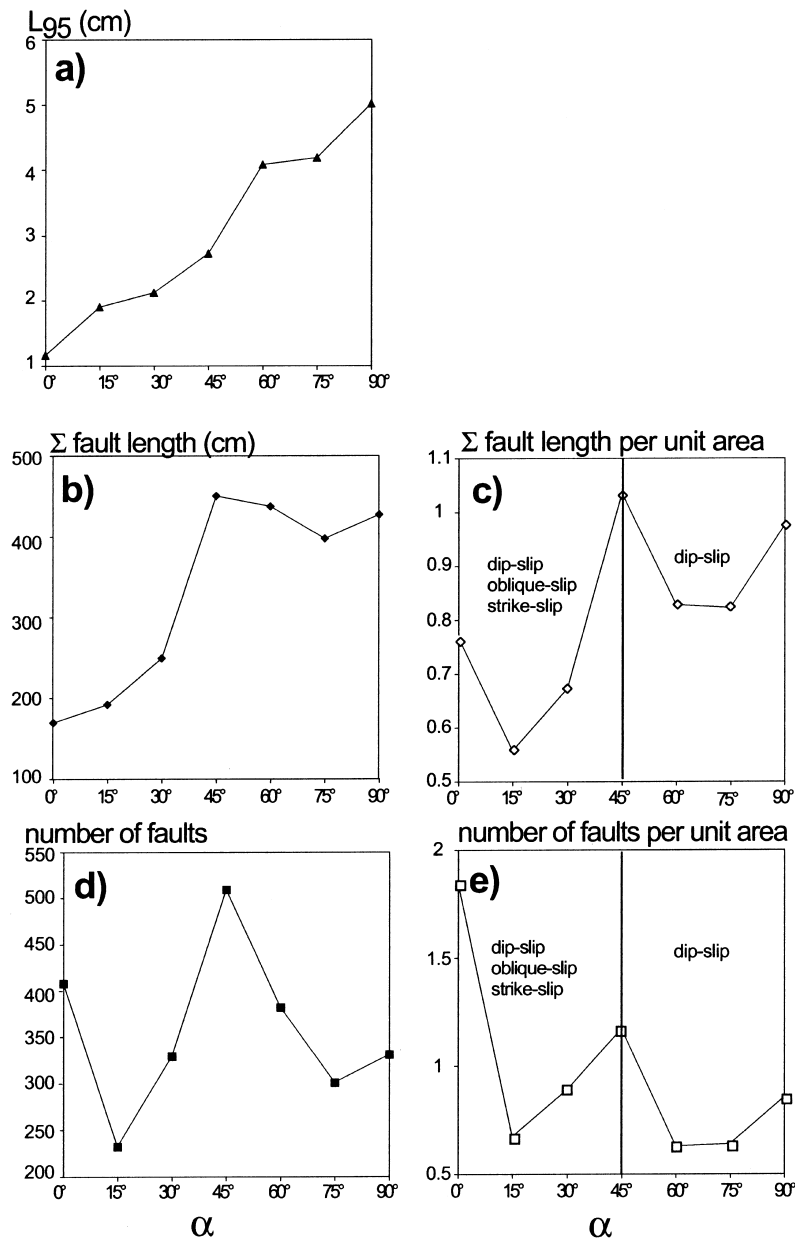

Fig. 14. Graphs showing how (a) the length of the fault at the 95th percentile of lengths, (b) summed fault length, and (d) number of faults vary with α. (c) Summed fault length per unit area. (e) Number of faults per unit area. See text for discussion.

ferently. On the same plots, we show the cumulative frequency for fault segments (as determined by the criteria described in Section 4.2). These data are fit very well by an exponential distribution for all values of α.

Not surprisingly, L_c for whole faults increases with increasing α in the same manner as does L_{95} (see Fig. 16). Alternatively, L_c for fault segments remains approximately the same for all values of α. Some studies suggest that segment length is controlled by mechanical layer thickness (Jackson and White, 1989; Scholz and Contreras, 1998). Our results suggest that one or more of the boundary conditions or material properties may control the length of fault segments, but it is fault geometry that controls how those segments link to form longer faults.

5. Discussion

5.1. Fault linkage

Withjack and Jamison (1986) determined, both

empirically and analytically, how stress and strain states vary with rift obliquity. In the analytical models, for all values of α, two of the principal stresses are horizontal and one is vertical. One of the horizontal principal stresses is tensional, and as α increases from $0°$ to $90°$, the angle between the rift trend and the principal stress also increases. For $\alpha \geq 45°$, both of the horizontal principal stresses are tensional (the vertical principal stress is always 0); for $\alpha \leq 30°$, one of the horizontal principal stresses is tensional whereas the other principal horizontal stress is compressional. Such stress states explain why so many of the major changes occur between $\alpha = 30°$ and $\alpha = 45°$. They also provide an explanation for fault geometry and for the variation in the number and length of faults with α. The clay, like rock, is weaker under tension than compression. When $\alpha \leq 30°$, the models are in compression and it is more difficult for faults to nucleate and lengthen. Hence, fault number and summed fault length are expected to be low. When $\alpha \geq 45°$, both horizontal stresses are tensional and faults can nucleate and grow more easily. The transition from a domain of dip-slip,
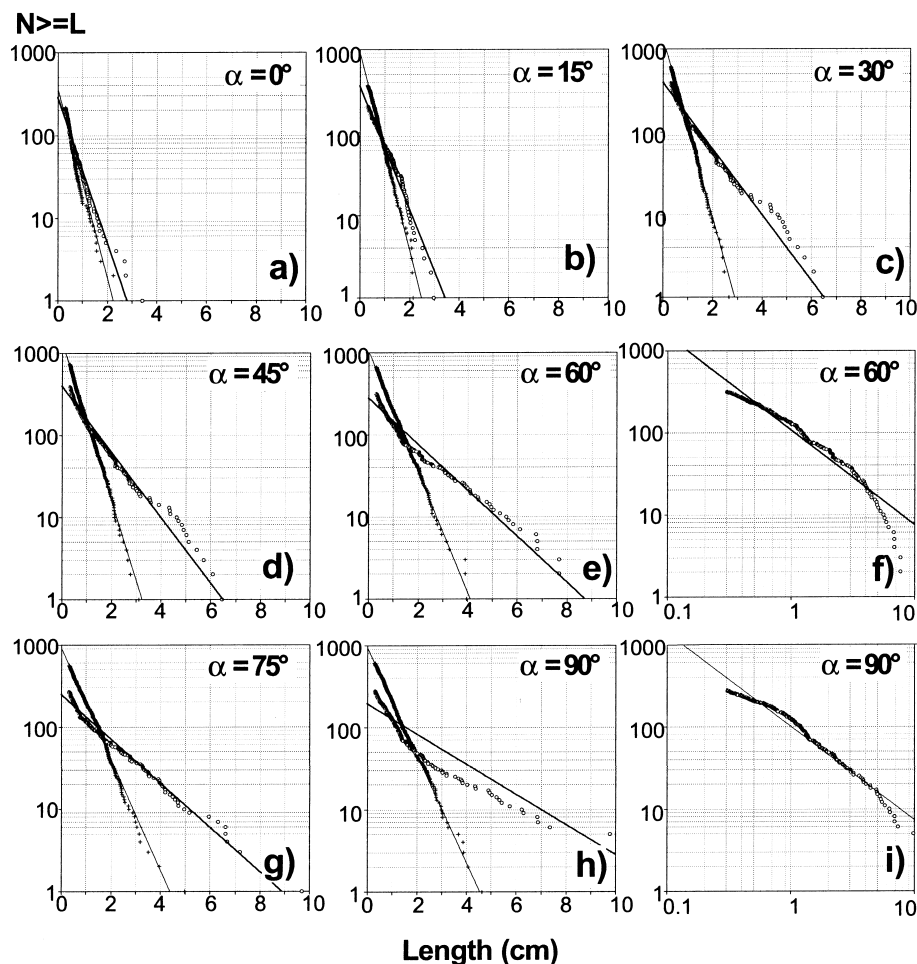

Fig. 15. Graphs showing cumulative frequency of lengths for whole faults (open circles) and for fault segments (crosses). (a–e), (g) and (h) Log-linear plots showing exponential fits. (f) and (i) Log–log plots showing power-law fits.

oblique-slip and strike-slip faulting to one of purely dip-slip faulting occurs at $\alpha = 45°$ (see Fig. 14). Whereas the number of faults is maximum at $\alpha = 45°$ and decreases when $\alpha = 60°$, fault length (L_{95}) almost doubles. We believe this occurs as extensional strain reaches a critical threshold after which growth by linkage dominates over growth by tip propagation, and fault nucleation either decreases considerably or ends all together. Rifts that are less oblique (i.e. have a higher value of α) have more extensional strain at a given displacement increment than highly oblique rifts (i.e. having a lower value of α; see Fig. 17). By the displacement increment analyzed in this study, models for $\alpha \geq 60°$ have experienced enough extension to have passed this threshold.

The kinematics of faulting in each model also has an influence on how much linkage can occur. Faults are overwhelmingly dip-slip in these models, with little evidence of oblique-slip (i.e. slickenlines on fault surfaces show only dip-slip motion). For $\alpha = 0°$ and $15°$ faults are predominantly conjugate strike-slip faults, with rift-subparallel faults having left-lateral offset and displacement-normal faults having right-lateral offset. These faults cannot share a slip vector and, therefore, truncate against one another and do not interact. In the few instances where the two sub-populations of faults interact and link in the $\alpha = 15°$ model, a significant dip-slip component develops once linkage has occurred and the now normal fault exhibits a near

right-angle bend. It is unclear why this should happen in a predominantly strike-slip model. One possibility is that, during linkage, faults rotate to an orientation more favorable for dip-slip motion. For $\alpha = 30°$, rift-subparallel faults exhibit left-oblique slip, whereas displacement-normal faults exhibit right-oblique slip. The geometry and kinematics of these faults allows some dip-slip motion to continue after they link. Faults in this model are highly complex and anastomosing, with many right-angle bends.

5.2. Spatial pattern of faults

Despite the lack of pre-existing anisotropy in our models, faults spontaneously develop in domains of uniform dip. Small faults are more abundant in the zone where faults of opposing dips have met. This can be seen best in our $\alpha = 45°$ model (Fig. 18). The most likely explanation for this apparent clustering is as follows: as the fault population evolves, small faults grow by tip propagation until they interact with other faults and link to form longer faults which continue growing. However, when the tips of faults having opposing dips meet, many of the faults lock, unable to gain either length or displacement. New faults must then nucleate in order to take up the continued strain imposed on the model.

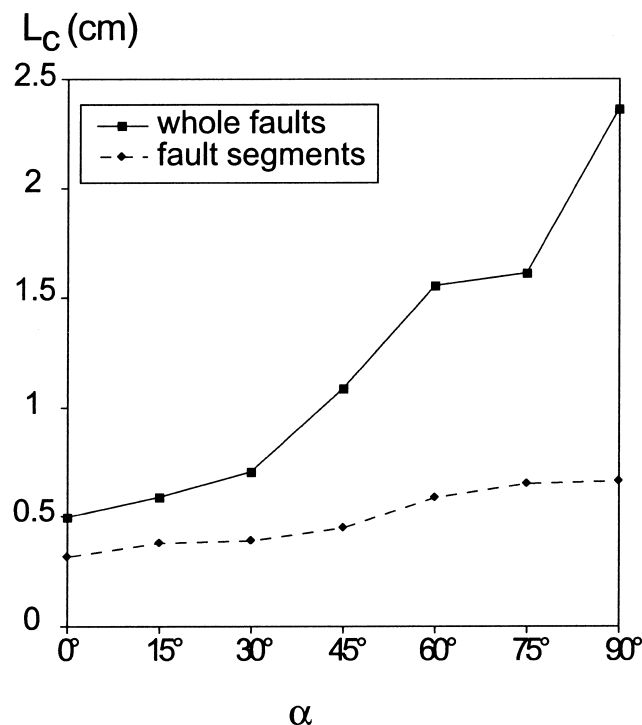The azimuths of small faults at a given α span the

Fig. 16. Graph showing variation in characteristic length (L_c) with a for whole faults (large squares) and fault segments (small circles).
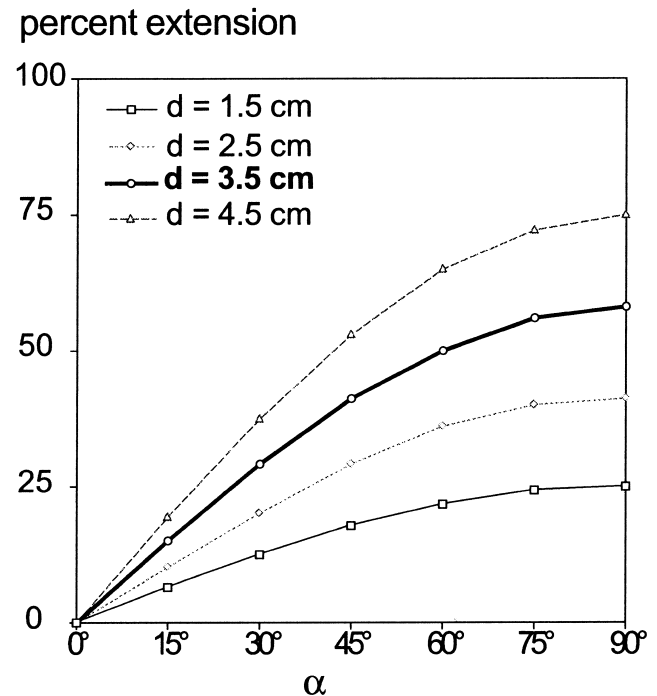

Fig. 17. Graph showing how imposed horizontal extensional strain in the displacement direction at the base of the model varies with α at different displacement increments during fault population evolution.

full range of the population, yet the longest faults all have the dominant trend. Possible explanations include the following: 1) small faults form with a wide distribution of azimuths but only those which are favorably oriented grow to significant length; 2) at low α values, faults rotate about a vertical axis as they lengthen; 3) small faults with a rift-parallel orientation form late during population evolution and do not have a chance to grow longer; or 4) small faults of every orientation link up and attain an 'average' azimuth as they lengthen. We suspect that all of these play a part. Evidence for the fourth alternative comes from the fact that the range of azimuth for segments is greater than that for whole faults. The fact that fault tortuosity has a general tendency to increase with fault length further supports this hypothesis.

In general, small faults tend to cluster both around fault tips and at the rift margins on all models where $\alpha \geq 30°$. Small faults that form at the rift margins are associated with a flexure that forms in the clay above the boundary between the latex sheet and the metal plate. This flexure becomes more pronounced as extension progresses and the center of the rift zone thins and subsides. The pattern of faulting at the rift margins in our oblique models is in fact similar to the secondary fault pattern produced by oblique-slip over a master fault. Using experimental models, Schlische et al. (1999) observed this pattern develop as faults cut an extensional forced fold (monoclinal flexure) which forms over a basement fault experiencing oblique-slip. These authors noted that relay ramps between the faults are not breached until displacement on the master fault is large. Thus, the faults do not lengthen by linkage and remain short as a result. We believe the same thing is happening in our models, but on a smaller scale at the rift margin.

5.3. Cumulative frequency distribution

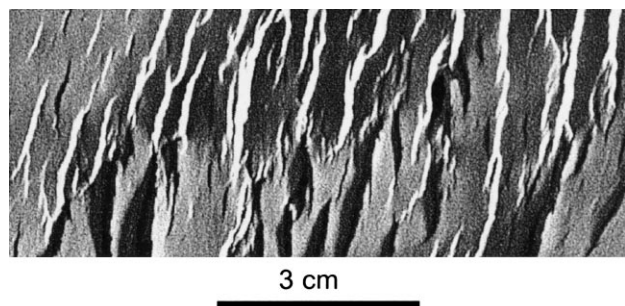Before fitting our cumulative frequency distributions, we eliminated truncated data at the small size

Fig. 18. Detail from a photograph of the $\alpha = 45°$ model showing the zone of complex faulting that forms where dip domains of opposite polarity meet.

3 cm

end of the distribution. We are confident that our data for models of $\alpha \geq 30°$ do not suffer from censoring at the large end of fault sizes. Because we are sampling experimental models in which we can see the entire population (above the imaging resolution), we know that there are no faults larger than the ones we can see and that we are sampling all faults present. The only faults that were not included in the analyses are those that formed in the area affected by boundary conditions at the edges of the apparatus. We believe that the manner in which the number of long faults in our models decreases is a result of boundary conditions imposed by the geometry of the rift. It is notable that, except for in the $\alpha = 90°$ model, the longest faults stop lengthening well before reaching the edge of the model and that the length of the longest faults increases with α. In fact, it is the geometry of the rift zone which limits fault length. If faults trend obliquely to the rift axis they either stop lengthening or begin to curve when they reach the rift valley walls. This may explain why a power-law size distribution is not appropriate for our data and perhaps not appropriate for fault populations in all oblique rift zones. It may also be the reason why it is the high end of our data that diverges most from the best-fit exponential curve (see Fig. 15).

In oblique rift zones, the geometry of the rift and the resulting trends of the faults have the greatest influence on how faults link. Therefore, it is not surprising that the cumulative frequency distribution of lengths varies with rift obliquity. The fact that characteristic length (L_c) for fault segments does not change significantly with α implies that it is indeed how these segments combine which determines the cumulative frequency distribution for whole faults. An exponential distribution fits our data for fault segments significantly better than data for whole faults. Davy (1993) describes a similar relationship in the San Andreas fault system where he found that small fault 'strands' related to the larger fault system follow an exponential distribution whereas the fault system as a whole does not.

5.4. Geological examples: continental rifts

Withjack and Jamison (1986) applied results of their experimental and analytical models to explain successfully fault patterns in the Gulf of Aden and the Gulf of California. Additional, more recent detailed field data from the Gulf of California (e.g. Umhoefer and Stone, 1996) provided support of those models. In continental rift zones, much of the deformation from rifting is controlled by pre-existing anisotropies in the underlying rocks. Such anisotropies are not present in the clay layers of our models. However, in the broadest sense, the edge of the overlapping metal plate in our models represents a very large-scale anisotropy

that controls the rift-zone geometry. Thus, at the largest scale, the modeling is an appropriate tool to understand the geometry of oblique continental rifts. Fault patterns similar to those in our models occur in continental rift zones that have localized along pre-existing tectonic trends oblique to the direction of absolute plate motion. The locations discussed below are shown in Fig. 19. The Connecticut Valley rift basin localized along a northerly trending tectonic grain during Triassic rifting, when displacement between North America and Africa was approximately NW–SE (e.g. Withjack et al., 1998; Fig. 20a). Two trends of normal faults were identified in the basin fill adjacent to the northerly trending border fault, one approximately 20° oblique to the trend of the border fault and the other approximately displacement normal (Clifton, 1987). deBoer and Clifton (1988) proposed that more northerly trending faults formed above weaknesses in the basement early in the basin history, and rotated slightly in response to far-field stresses as they propagated upward into the basin fill. More northeasterly trending, displacement-normal faults developed later, in the basin fill, and became the predominant fault trend in the center of the basin.

Færseth et al. (1997) offered a similar interpretation of the fault pattern in the northern North Sea (Fig. 20b), where basins localized along northerly trending Permian structures during NW–SE extension in the Jurassic. Early basin-parallel faults formed coevally with small northeast-trending faults, but a northeast-trending fault set predominates later in basin evolution. Færseth et al. (1997) reject the notion that a change in stress direction is required to produce the two sets of faults present in the northern North Sea. Our models support their conclusion. When rotated into the same orientation as these basins, the fault geometry in our $\alpha = 75°$ model looks similar to both of the above examples. Once again, it is a difference in boundary conditions between the rift margin and the center of the rift zone that results in two fault sets forming during oblique extension.

5.5. Geological examples: oblique mid-ocean ridge segments

Scaled physical models have been used to interpret the geometry and evolution of fracture populations that form on mid-ocean ridges during oblique extension. Dauteuil and Brun (1993, 1996) compared their sand over putty models to the Mohns Ridge, which is 45° oblique to the spreading direction. Applegate and Shor (1994) compared fracture data for the Reykjanes Ridge to the clay models of oblique rifting of Withjack and Jamison (1986) and the sand-over-putty models of Tron and Brun (1991). All authors noted that the scaled models accurately predict the fault geometry that is present on these oblique ridge segments. Tuckwell et al. (1996) note that a transtensional model, supported by the clay models of Withjack and Jamison (1986), best matches the features of oblique ridge segments on slow-spreading ridges.

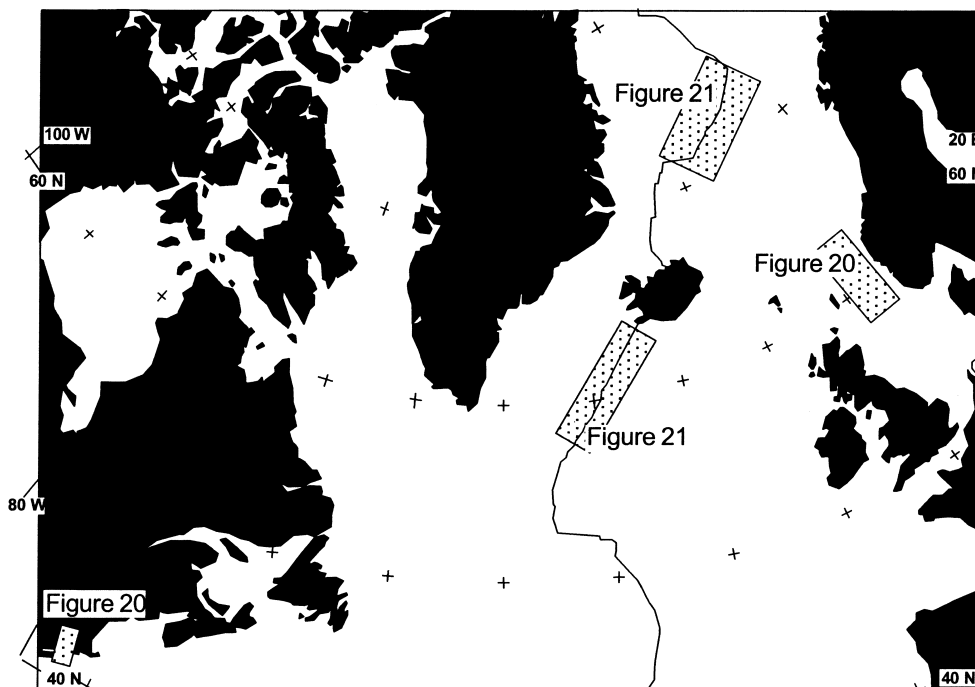The fault patterns on our models compare well with

Fig. 19. Location map showing field examples of oblique rift zones (redrawn and simplified from Vogt, 1986).

fault patterns described on oblique mid-ocean ridge segments. Our models represent distributed deformation of a relatively thin brittle layer above a narrow discontinuity that deforms continuously. This is analogous to the deformation observed at mid-ocean ridges which comprises normal faults, opening mode fissures, and dike-induced grabens narrowly distributed over a volcanic zone. Although all brittle deformation in our models is accommodated by normal faults, the geometry and distribution of fractures is comparable to that at ridges. Although the models cannot reproduce the deformation resulting from magma injection, they can predict the fracture pattern that results exclusively from far-field tectonic stresses. The models are particularly useful analogues for slow-spreading ridges, where faulting contributes significantly to extension (Cowie et al., 1993a).

Dauteuil and Brun (1996) described a pattern of complex, wavy and anastomosing faults in the axial valley of the Mohns Ridge in the North Atlantic ($\alpha = 45$–$50°$). They noted that faults along the rift valley walls are short and slightly oblique to the rift trend, whereas faults in the rift valley are longer, less complex and trend normal to the spreading direction. They also described 'spindle' and 'y-type' connections resulting from linkage of faults with different azimuths. They interpret the en-échelon pattern of faults at the valley walls as evidence of strike-slip displacement but present no evidence of actual offset. Our $\alpha = 45°$ model has similar fault geometries, with short faults trending slightly oblique to rift-parallel on the margins of the deformed zone and longer displacement-normal faults in the center of the rift zone. The greatest complexity

occurs where these two fault sets interact near the southern (lower) rift margin (see Fig. 21a and b). Faults at the rift margin exhibit en-échelon geometry, but all displacement is pure dip-slip. In fact, there is no evidence of strike-slip displacement anywhere in this model.

McAllister et al. (1995) described a wide distribution of fault azimuths along the Reykjanes Ridge ($\alpha = 60$–$65°$) with a spatial distribution of faults similar to our $\alpha = 60°$ model (Fig. 21c and d). Faults within the rift valley trend nearly normal to the spreading direction whereas faults along the rift walls are long and trend parallel to the rift axis. Histograms of fault trends on the Reykjanes Ridge (McAllister et al., 1995; see their figure 10) show that faults at the rift margin have a wider range of azimuth than faults in the center of the rift, and that many faults are oblique to the rift trend. The authors suggested that faults form in the center of the rift as a result of plate-spreading stresses, whereas, on the edge of the rift, they form under a distinct stress system oriented perpendicular to the rift axis. They proposed that this stress develops as a result of lithospheric cooling away from the ridge axis. In our models, the zone of faulting at the rift margin has a rift-parallel trend, and the longest faults in this zone do indeed have a rift-parallel trend. However, the majority of faults are short and trend as much as $10°$ oblique to the rift axis. We believe that they are forming as a result of a secondary stress system localized along the flexure that develops where the latex sheet is joined to the metal plate (i.e. where boundary conditions have changed). We agree that lithospheric cooling and resulting gravitational effects are probably
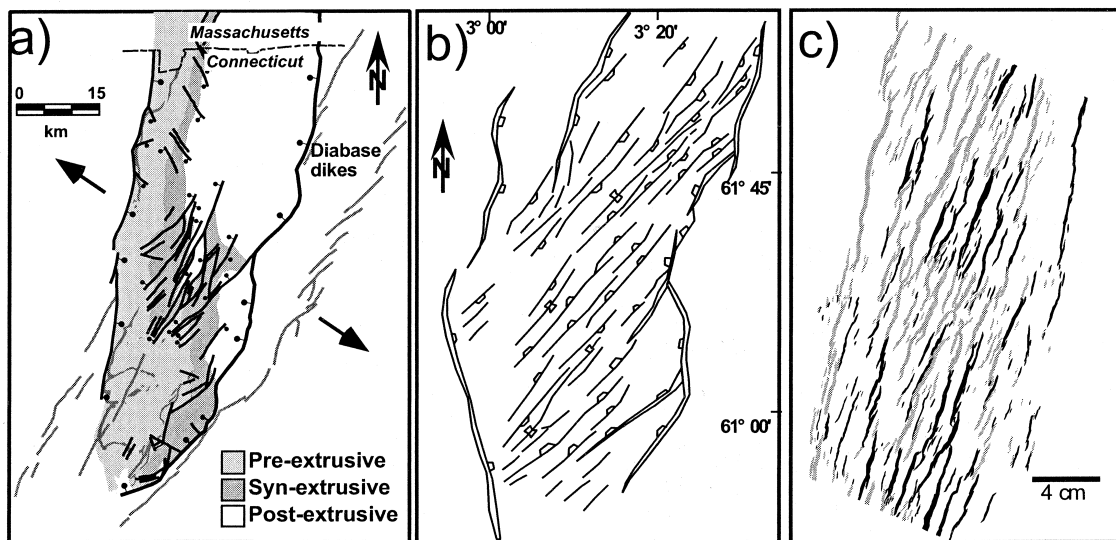

Fig. 20. Comparison of map patterns of faults in oblique continental rift basins with fault trace map of our clay model. (a) Faults in the Hartford sub-basin, Connecticut, simplified from Schlische (1993). (b) Faults in the Viking Graben, northern North Sea (redrawn from Færseth et al., 1997). (c) Fault trace map of our $\alpha = 75°$, flipped horizontally and rotated into the same position with respect to the displacement direction as the basins above.

responsible for the fault pattern at the walls of the Reykjanes and Mohns Ridges. We suggest that stresses related to plate motion are modulated and reoriented by a secondary stress field related to changes in topography and crustal rheology at the rift valley walls. It is the interaction of these two stress systems that causes faults to strike oblique to the rift trend rather than parallel to it.

6. Summary and conclusions

Clay experimental models have been used to simulate fault population systematics in oblique rift zones. The following parameters of fault populations vary systematically with rift obliquity.

1) The range of fault azimuths increases as rift obliquity increases (i.e. as α decreases). For values of $\alpha \geq 45°$, faults at the rift margin are slightly oblique to the rift trend, whereas faults in the center of the rift are slightly oblique to the displacement-normal direction. All faults experience dip slip. When $\alpha \leq 30°$, two fault populations of equal importance develop in the center of the rift: one approximately rift parallel and the other approximately displacement normal. Faults in these models experience dip-slip, oblique-slip and strike-slip motion.

2) The fractal dimension of the spatial pattern of faults increases as α increases and is comparable to values derived analytically (Takayasu, 1986) and measured in the field (Hirata, 1989).

3) The length of the longest faults and the width of the deformed zone both increase as α increases.

4) The cumulative frequency distribution of fault lengths varies with α. The cumulative frequency does not follow a power-law for any of our models, with the possible exception of $\alpha = 90°$. An exponential distribution best describes our data for whole fault and fault segment lengths. L_c for whole faults increases as α increases, but L_c for fault segments remains relatively unchanged.

Several parameters vary due to fault linkage.

1) For all oblique rifts dominated by normal faulting, fault tortuosity increases with fault length. This is a result of linkage between short fault segments with a broad range of azimuths.
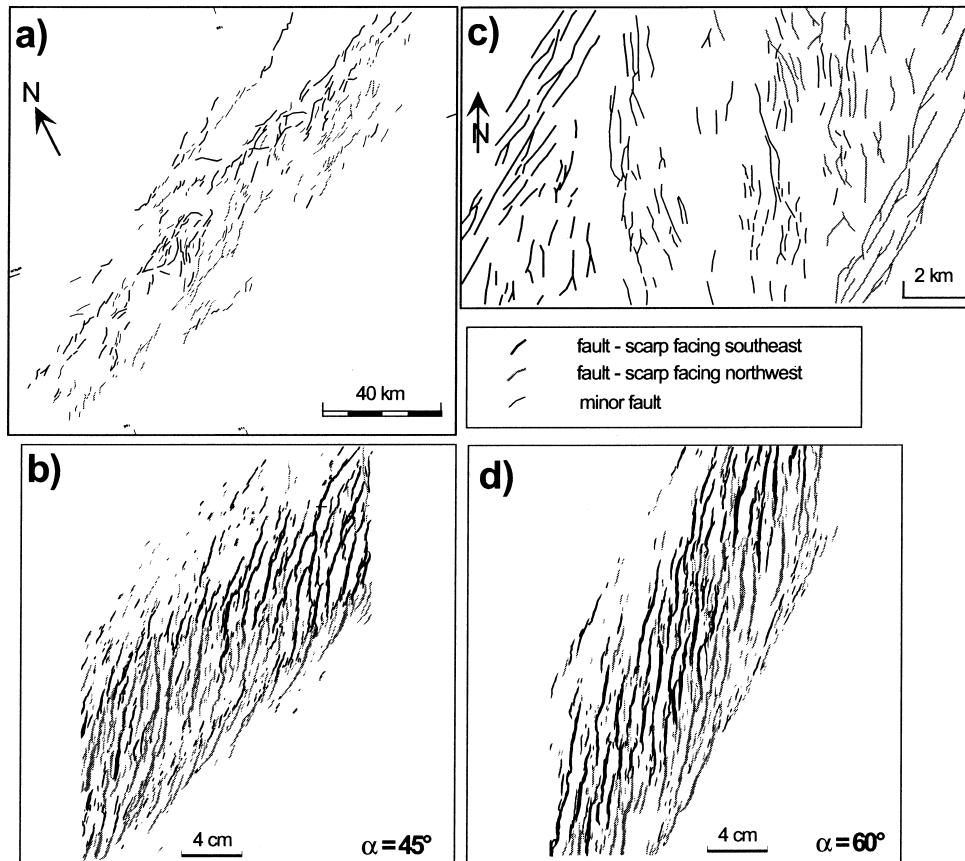

Fig. 21. Comparison of map patterns of faults on oblique mid-ocean ridge segments with fault trace maps of our clay models. (a) Faults on the Mohns Ridge (redrawn from Dauteuil and Brun, 1996). (b) Fault trace map for $\alpha = 45°$. (c) Faults on a small section of the Reykjanes Ridge (redrawn from McAllister et al., 1995). (d) Fault trace map for $\alpha = 60°$. All maps are oriented so that the spreading (displacement) direction is perpendicular to the side of the box.

2) Fault tortuosity is maximum when $\alpha = 30°$ as two subpopulations of faults link.

3) The greatest increase in fault number, at $\alpha = 45°$, is followed by almost as great a decrease at $\alpha = 60°$ and is coincident with the greatest increase in the length of the longest faults. This change occurs after a critical strain threshold is reached. Subsequently, most fault growth is accomplished by linkage. Simultaneous increase in fault length and decrease in fault number characterize such an event.

Many of the characteristics of fault populations that we observe in our models have been described at oblique segments of the Mid-Atlantic Ridge, including the Mohns Ridge and the Reykjanes Ridge. A secondary stress system forms at the rift margins in response to a change in boundary conditions. Interaction of two stress systems causes faults in that zone to strike oblique to the rift trend, whereas faults that are approximately displacement-normal form in the center of the rift zone. Our models reproduce the geometry of faults described in continental rift zones such as the Connecticut basin and the basins of the northern North sea, which localized along pre-existing tectonic trends oblique to the direction of displacement. Our models also provide good analogs for characterizing brittle deformation at mid-ocean ridges where homogeneous, relatively thin crust is being deformed by tensional forces in a confined rift zone where the spreading vector is known. The geometry and spatial distribution of faults in oblique rift zones are predictable and are a function of the angle between the rift trend and the direction of displacement. The characteristic length of fault segments that form in the rift does not vary with α, but the manner in which those segments link to form longer faults is a function of rift obliquity.

Acknowledgements

References

Ackermann, R.V., Schlische, R.W., 1997. Anticlustering of small normal faults around larger faults. Geology 25, 1127–1130.

Ackermann, R.V., Schlische, R.W., Withjack, M.O., 1997. Systematics of an evolving population of normal faults in scaled physical models. Geological Society of America Abstracts with programs A-198.

Angelier, J., Bergerat, F., 1983. Systemes de contrainte et extension intracontinentale. Societe Nationale Elf Acquitaine (Production) F-64018, 137–147.

Applegate, B., Shor, A.N., 1994. The northern Mid-Atlantic and Reykjanes Ridges: spreading center morphology between 55°50′N and 63°00′N. Journal of Geophysical Research 99, 17935–17956.

Aviles, C.A., Scholz, C.H., Boatwright, J., 1987. Fractal analysis applied to characteristic segments of the San Andreas Fault. Journal of Geophysical Research 92, 331–344.

Cartwright, J.A., Trudgill, B.D., Mansfield, C.S., 1995. Fault growth by segment linkage: an explanation for scatter in maximum displacement and trace length data from the Canyonlands. Journal of Structural Geology 17, 1319–1326.

Chorowicz, J., Sorlien, C., 1992. Oblique extensional tectonics in the Malawi Rift, Africa. Geological Society of America Bulletin 104, 1015–1023.

Cladouhos, T.T., Marrett, R., 1996. Are fault growth and linkage models consistent with power-law distributions of fault lengths? Journal of Structural Geology 18, 281–293.

Clifton, A.E., 1987, Tectonic analysis of the western border fault zone of the Mesozoic Hartford Basin, Connecticut and Massachusetts, M.A. thesis, Wesleyan University.

Clifton, A.E., Schlische, R.W., 1997. Using scaled physical models of oblique deformation to analyze the spatial and temporal evolution of fault systems. Geological Society of America Abstracts with Programs A-258.

Clifton, A.E., Schlische, R.W., Withjack, M.O., Ackermann, R.V., 1998. Using scaled physical models of oblique extension to study the temporal evolution of segmented fault systems. EOS Transactions of the Geological Society of America 79, F648.

Cowie, P.A., 1998. A healing–reloading feedback control on the growth rate of seismogenic faults. Journal of Structural Geology 20, 1075–1087.

Cowie, P.A., Scholz, C.H., 1992. Physical explanation for displacement–length relationship of faults using a post-yield fracture mechanics model. Journal of Structural Geology 14, 1133–1148.

Cowie, P.A, Knipe, R.J., Main, I.G., 1996. Introduction to the Special Issue. Journal of Structural Geology 18, v–xi.

Cowie, P.A., Sornette, D., Vanneste, C., 1995. Multifractal scaling properties of a growing fault population. Geophysical Journal International 122, 457–469.

Cowie, P.A., Scholz, C.H., Edwards, M., Malinverno, A., 1993a. Fault strain and seismic coupling on mid-ocean ridges. Journal of Geophysical Research 98, 17911–17920.

Cowie, P.A., Vanneste, C., Sornette, D., 1993b. Statistical physics model for the spatiotemporal evolution of faults. Journal of Geophysical Research 98, 21809–21821.

Dauteuil, O., Brun, J.-P., 1993. Oblique rifting in a slow-spreading ridge. Nature 361, 145–148.

Dauteuil, O., Brun, J.-P., 1996. Deformation partitioning in a slow spreading ridge undergoing oblique extension. Mohns Ridge, Norwegian Sea. Tectonics 15, 870–884.

Davy, P., 1993. On the frequency–length distribution of the San Andreas Fault System. Journal of Geophysical Research 98, 12141–12151.

Dawers, N.H., 1996, Observations of fault growth scaling relations. Ph.D. thesis, Columbia University.

deBoer, J.Z., Clifton, A.E., 1988. Mesozoic tectogenesis. development and deformation of 'Newark' rift zones in the Appalachians (with special emphasis on the Hartford basin, Connecticut). In: Manspeizer, W. (Ed.), Triassic–Jurassic Rifting, Continental Breakup and the Origin of the Atlantic and Passive Margins, Part A, Developments in Geotectonics, 22. Elsevier, Amsterdam, pp. 275–302 (*published as deBoer and Clifford, due to editing error).

Færseth, R.B., Knudsen, B.-E., Liljedahl, T., Midbøe, P.S., Søderstrøm, B., 1997. Oblique rifting and sequential faulting in the Jurassic development of the northern North Sea. Journal of Structural Geology 19, 1285–1302.

Hatton, C.G., Main, I.G., Meredith, P.G., 1994. Non-universal scaling of fracture length and opening displacement. Nature 367, 160–162.

Hirata, T., 1989. Fractal dimension of fault systems in Japan: Fractal structure in rock fracture geometry at various scales. PAGEOPH 131, 157–170.

Hubbert, M.K., 1937. Theory of scale models as applied to the study of geologic structures. Geological Society of America Bulletin 48, 1459–1520.

Jackson, J.A, White, N.J., 1989. Normal faulting in the upper continental crust: observations from regions of active extension. Journal of Structural Geology 11, 15–36.

Kautz, S.A., Sclater, J.G., 1988. Internal deformation in clay models of extension by block faulting. Tectonics 7, 823–832.

Lindholm, R.C., 1978. Triassic–Jurassic faulting in eastern North America—a model based on pre-Triassic structures. Geology 6, 365–368.

McAllister, E., Cann, J., Spencer, S., 1995. The evolution of crustal deformation in an oceanic extensional environment. Journal of Structural Geology 17, 183–199.

McClay, K.R., White, M.J., 1995. Analogue modelling of orthogonal and oblique rifting. Marine and Petroleum Geology 12, 147–151.

Main, I., 1996. Statistical physics, seismogenesis, and seismic hazard. Reviews of Geophysics 34, 433–462.

Morley, C.K., 1995. Developments in the structural geology of rifts over the last decade and their impact on hydrocarbon exploration. In: Lambiase, J.J. (Ed.), Hydrocarbon Habitat in Rift Basins, Geological Society Special Publication, 80, pp. 1–32.

Moustafa, A.D., 1996. Internal structure and deformation of an accommodation zone in the northern part of the Suez rift. Journal of Structural Geology 18, 93–107.

Murton, B.J., Parson, L.M., 1993. Segmentation, volcanism and deformation of oblique spreading centers: a quantitative study of the Reykjanes Ridge. Tectonophysics 222, 237–257.

Mutter, J.C., Karson, J.A., 1992. Structural processes at slow-spreading ridges. Science 257, 627–634.

Okobu, P.G., Aki, K., 1987. Fractal geometry in the San Andreas fault system. Journal of Geophysical Research 92, 345–355.

Pickering, G., Bull, J.M., Sanderson, D.J., 1995. Sampling power-law distributions. Tectonophysics 248, 1–20.

Schlische, R.W., 1993. Anatomy and evolution of the Triassic–Jurassic continental rift system, eastern North America. Tectonics 12, 1026–1042.

Schlische, R.W., Anders, M.H., 1996. Stratigraphic effects and tectonic implications of the growth of normal faults and extensional basins. In: Beratan, K.K. (Ed.), Reconstructing the structural history of basin and range extension using sedimentology and stratigraphy, Geological Society of America Special Paper, 303, pp. 183–203.

Schlische, R.W., Withjack, M.O., Eisenstadt, G., 1999. An experimental study of the secondary fault patterns produced by oblique-slip faulting. EOS Transactions of the Geological Society of America 80, S339.

Scholz, C.H., Contreras, J.C., 1998. Mechanics of continental rift architecture. Geology 26, 967–970.

Sornette, D., Davy, P., Sornette, A., 1990. Structuration of the lithosphere in plate tectonics as a self-organized critical phenomenon. Journal of Geophysical Research 95, 17353–17361.

Takayasu, H., 1986. Pattern formation of dendritic fractals in fracture and electrical breakdown. In: Pietronero, L., Tosattic, E. (Eds.), Fractals in Physics. Elsevier, Amsterdam, pp. 181–184.

Tron, V., Brun, J.-P., 1991. Experiments on oblique rifting in brittle–ductile systems. Tectonophysics 188, 71–84.

Trudgill, B., Cartwright, J., 1994. Relay ramp morphologies and normal fault linkages, Canyonlands National Park, Utah. Geological Society of America Bulletin 106, 1143–1157.

TruSoft International, 1997, Benoit v. 1.1, St. Petersburg, Florida.

Tuckwell, G.W., Bull, J.M., Sanderson, D.J., 1996. Models of fracture orientation at oblique spreading centres. Journal of the Geological Society of London 153, 185–189.

Umhoefer, P.J., Stone, K.A., 1996. Description and kinematics of the SE Loreto basin fault array, Baja California Sur, Mexico: a positive field test of oblique-rift models. Journal of Structural Geology 18, 595–614.

Vogt, P.R., 1986. The present plate boundary configuration. In: Vogt, P.R., Tucholke, B.E. (Eds.), The Geology of North America, Volume M, The Western North Atlantic Region. Geological Society of America, pp. 189–204.

Withjack, M.O., Callaway, J.S., 2000, Active normal faulting beneath a salt layer: An experimental study of deformation in the cover sequence. American Association of Petroleum Geologists Bulletin, in press.

Withjack, M.O., Jamison, W.R., 1986. Deformation produced by oblique rifting. Tectonophysics 126, 99–124.

Withjack, M.O., Schlische, R.W., Olsen, P.E., 1998. Diachronous rifting, drifting and inversion on the passive margin of eastern North America: An analog for other passive margins. American Association of Petroleum Geologists Bulletin 82, 817–835.

Wojtal, S.F., 1996. Changes in fault displacement populations correlated to linkage between faults. Journal of Structural Geology 18, 265–279.